Published in final edited form as:
Hear Res. 2010 September 1; 268(1-2): 172–183. doi:10.1016/j.heares.2010.05.019.

In vitro effects of recombinant Otoconin 90 upon calcite crystal growth. Significance of tertiary structure

Wenfu Lu[a], **Dan Zhou**[b], **John J. Freeman**[c], **Isolde Thalmann**[a], **David M. Ornitz**[d], and **Ruediger Thalmann**[a,*]

[a]Department of Otolaryngology-Head and Neck Surgery, Washington University in St. Louis, Campus Box 8115, 660 South Euclid Avenue, St. Louis, MO 63110 USA.

[b]Center for Nanoscience, University of Missouri-St. Louis, One University Boulevard, St. Louis, MO 63121 USA. zhouda@umsl.edu

[c]Department of Earth & Planetary Sciences, Washington University in St. Louis, Campus Box 1169, 1 Brookings Dr., Saint Louis, MO 63130-4862 USA. johnjfreeman@wustl.edu

[d]Department of Developmental Biology, Washington University in St. Louis, Campus Box 8103, 660 South Euclid Avenue, MO 63110 USA. dornitz@wustl.edu

Abstract

Otoconia are biomineral particles of microscopic size essential for perception of gravity and maintenance of balance. Millions of older Americans are affected in their mobility, quality of life and in their health by progressive demineralization of otoconia. Currently, no effective means to prevent or counteract this process are available. Because of prohibitive anatomical and biological constraints, otoconial research is lagging far behind other systems such as bone and teeth. We have overcome these obstacles by generating otoconial matrix proteins by recombinant techniques. In the present study, we evaluated the effects of recombinant Otoconin 90 (OC90), the principal soluble matrix protein upon calcite crystal growth patterns *in vitro*. Our findings highlight multiple effects, including facilitation of nucleation, and inhibition of crystal growth in a concentration-dependent manner. Moreover, OC90 induces morphologic changes characteristic of native otoconia.

OC90 is considerably less acidic than the prototypical invertebrate $CaCO_3$ –associated protein, but is nevertheless an effective modulator of calcite crystal growth. Based on homology modeling of the sPLA2-like domains of OC90, we propose that the lower density of acidic residues of the primary sequence is compensated by formation of major anionic surface clusters upon folding into tertiary conformation.

Keywords

Biomineralization; Otoconin 90; Otoconia

[*]**Corresponding author**: Ruediger Thalmann, M.D. Department of Otolaryngology Washington University School of Medicine 660 S. Euclid Avenue, Box 8115 St. Louis, MO 63110 USA Phone: 314-367-1968 Fax: 314-362-7568 thalmannr@ent.wustl.edu. luwenfu@gmail.com, thalmann_i@ent.wustl.edu.

1. Introduction

Otoconia are minute, high density biomineral particles overlying the sensory epithelia of the gravity receptor organ of the inner ear. They provide the inertial mass necessary for optimal perception of linear acceleration and gravity. The shearing motion between the otoconial complex and the hair cell stereocilia caused by head movement leads to bending of the hair cell cilia, which results in transduction of the mechanical stimulus into an electrical response, transmitted to the central nervous system.

Mammalian otoconia have a barrel-like shape with tri-planar end facets and average 5-10 μm in length. The organic core is surrounded by a mineral shell consisting of thousands of calcite crystallites arranged in a highly ordered mosaic (Mann et al., 1983). Otoconia are formed during late embryonic development and mature shortly after birth; they remain essentially stable thereafter (Veis, 2003;Kawamata and Igarashi, 1995;Erway et al., 1986;Thalmann et al., 2001). Otoconia are subject to injury by drugs, disease and trauma; the most important dysfunction, however, is progressive demineralization due to aging, ultimately resulting in degeneration with impairment or loss of balance, and susceptibility to falling and bone fracture. Balance-related falls are the leading cause of accidental deaths in the elderly population. Another pathologic entity, benign positional vertigo (BPV), which affects also younger age groups, results from translocation of otoconia into the semicircular canals rendering their receptors responsive to gravity. Consequently, changes in head position lead to severe vertigo and nausea. In spite of the significance of otoconial integrity in maintaining balance and the serious consequences of otoconial pathology, little is known about the processes underlying their formation and maintenance.

As biominerals, otoconia are formed according to the principles of biologically controlled mineralization (Mann, 2001). In this scheme, insoluble framework molecules specify the sites of nucleation and orientation of crystal growth, whereas soluble growth modulators manipulate the energy landscape such that minerals can be formed at ambient conditions (reasonable pressure, temperature, and pH).

With the availability of highly sensitive chemical analytical techniques and progress in molecular cloning technology, numerous otoconial matrix proteins have been identified. Otoconin 90 (OC90), the principal otoconial protein, which accounts for more than 90% of the soluble phase, was determined first (Wang et al., 1998;Verpy et al., 1999;Pote and Ross, 1991). The molecule contains two globular domains homologous to secretory phospholipase A2 (sPLA2) connected by a linker segment and framed by terminal extensions. The polypeptide backbone has a molecular weight of approximately 50 kDa and contains extensive post-translational modifications including N-linked saccharides and a major sulfated glycosaminoglycan (GAG) complement, as well as numerous phosphoryl groups, which together raise the molecular weight to approximately 100 kDa. OC90 is not expressed, as originally believed, by the macular sensory patches near the nascent otoconia, but by distantly located non-sensory epithelia. The protein is secreted at extremely high levels during a short time window of the late embryonic period, but drops precipitously thereafter (Verpy et al., 1999;Thalmann et al., 2001;Ignatova et al., 2004). Subsequently, several less abundant matrix proteins (minor otoconins) were identified, including fetuin A, osteopontin, laminin alpha 3, Sparc-like protein 1, and myosin regulatory light polypeptide 9, all calcium-binding proteins (Thalmann et al., 2006). Finally, the principal insoluble scaffold protein otolin-1 that had previously been documented and partially characterized in the otoliths of bony fish (teleosts), was identified in mouse otoconia and shown to be recruited into the otoconial matrix by OC90 (Zhao et al., 2007;Murayama et al., 2005). Otolin-1 is a novel collagenous molecule, homologous to collagen type X.

Identification and partial characterization of these molecules, however, did not provide the quintessential information – their role in mediation of otoconial mineralization. In other biomineral systems, the standard approach to address fundamental mechanistic issues consists of *in vitro* techniques, where each matrix protein is studied in isolation, and essential parameters controlling crystal growth modulation can be manipulated and assessed systematically. In virtually all biomineral systems, ranging from sea shells to cultures of magnetotactic bacteria, ample matrix protein can be extracted from the mineral phase. This powerful approach, however, has not been applicable to otoconia, because of the insufficient quantities of native protein available from the diminutive otoconial complex. Consequently, progress in the understanding of fundamental otoconial mechanism and corresponding pathologic processes has been severely limited. We overcame these obstacles by generating the necessary quantities of matrix protein by recombinant techniques, addressing in this first study the principal soluble matrix protein OC90. In view of the extensive post-translational modifications we relied upon mammalian expression. After validation of the biochemical authenticity of the recombinant protein and ascertaining proper folding, we initiated *in vitro* studies on the modulation of calcite crystal growth.

We demonstrate that OC90 is a multifunctional molecule which causes marked concentration-dependent facilitation of nucleation and inhibition of crystal growth, as well as morphologic modifications resulting in an otoconia-like shape. Solution state studies, combined with molecular modeling, provided initial insights into mechanisms controlling the growth kinetics of calcite. Analysis of homology-based molecular models of the sPLA2-like globular domains of OC90 identified putative two-dimensional functional regions at the solvent exposed molecular surfaces, including a six-unit anionic cluster surrounded by numerous hydrogen-bonding residues.

2. Materials and Methods

2.1 Construction of mouse rOC90

OC90 cDNA was amplified by RT-PCR using total RNA purified from E16.5 mouse otocysts. The sequences of upstream and downstream primers were: OC90 sense, 5’ GGT ACC GCC ACC ATG ATT ATG CTG CTC ATG GTC GG 3’, OC90 antisense, 5’ CTC GAG TTA ATG ATG ATG ATG ATG ATG TTT CCC ACC GAG GGG TCT GG 3’, respectively. OC90 sense had a Kozak sequence and a KpnI recognition site. OC90 antisense had an XhoI recognition site and a six Histidine tag sequence (underscored) before the stop codon. The fragment was subcloned into pGEMT-easy. The cDNA was then released by digestion with KpnI and XhoI and inserted into pcDNA3.1 (+). A point mutation (T to C) at 1264 nucleotide was corrected by overlap extension PCR with primers: 5’ CCT TCT TTA ATC AAA GCC TCA AGT CAC CAG ACG GAG CCG AGT G 3’ and 5’ CAC TCG GCT CCG TCT GGT GAC TTG AGG CTT TGA TTA AAG AAG G 3’. The cDNA sequence was confirmed by sequencing.

2.2 Protein expression and purification

For production of mouse OC90-6xHis proteins by human embryonic kidney (HEK293) cells, the expression plasmids pcDNA3.1-OC90-6xHis were stably transfected into HEK293 cells with Lipofectamine 2000. The transfected cells were incubated at 37 °C and 5% CO_2 in Dulbecco's Modified Eagle Medium supplemented with 10 % fetal bovine serum and 100 U/mL penicillin and 100 μg/mL streptomycin. On the following day cells were replaced with fresh medium containing 1 mg/mL G418 and allowed to grow for another two weeks. Neomycin-resistant clones were screened for high level expression of rOC90 by Western blot using polyclonal rabbit anti-mouse OC90 and monoclonal mouse anti-6xHis antibodies. HEK293 cells from two resistant clones with the highest level stable expression of rOC90

were grown to confluence in DMEM, complemented with 5% fetal bovine serum and 500 μg/mL G418, then replaced with EX-CELL 293 serum-free medium and allowed to grow in T-175 flasks for another 3 days. The conditioned medium was harvested and applied to Ni-NTA superflow resin in batch mode. The following purification step was performed according to the manufacturer's instructions with small modifications. Protein concentration was determined by the BCA (bicinchoninic acid) assay (Pierce). The purity and identity of the proteins were determined by Coomassie staining and Western blot using monoclonal mouse anti-6xHis antibody (1:3000) and polyclonal rabbit anti-mouse OC90 antibody (3 μg/mL) following a 7.5 ~ 10% SDS-polyacrylamide gel electrophoresis.

2.3 Glycosylation of rOC90

N-glycosylation of rOC90 was determined by enzymatic deglycosylation using N-glycosidase F. Briefly, 25 μg of protein was added to a microcentrifuge tube and adjusted to a final volume of 35 μl with water. Ten μl of 250 mM phosphate buffer, pH 7.5, and 2.5 μl of 2% SDS with 1 M 2-mercaptoethanol were added to the tube, which was then heated at 95 °C for 5 minutes and cooled. Subsequently, 2.5 μl of 5% (v/v) Triton X-100 were added and mixed. Finally all samples treated with or without 2.0 μl of the N-glycosidase F solution were incubated at 37 °C for 16 hours. The amount of glycosylation was estimated from the reduction of the molecular weight. The presence of acidic GAG of rOC90 was assayed by alcian blue staining as described (Wall and Gyi, 1988).

2.4 Crystal growth and scanning electron microscopy

Calcite crystals were grown by slow evaporation of NH_4HCO_3 into a $CaCl_2$ solution as reported (Lakshminarayanan et al., 2002;Albeck et al., 1993). Briefly, calcite crystals were grown on clean glass cover slips, placed into wells of a cell culture dish containing the growth solution. The whole set-up was covered with aluminum foil with a few pin holes, and placed into a desiccator containing NH_4HCO_3. Protein aliquots were dissolved in 7.5 mM $CaCl_2$ and crystals were grown for 48 hours. Crystals were examined with a JEOL JSM 6320F Field Emission scanning electron microscopy at 5 KV after sputter coating with gold and palladium to increase the conductivity.

2.5 Raman spectral analysis

Raman spectra were collected on pre-selected grains of $CaCO_3$ with a HoloLab 5000 Raman microprobe spectrometer system (Kaiser Optical Systems, Inc., KOSI), using a 532 nm, frequency-doubled, Nd:YAG solid-state laser as the excitation source, and a holographic grating spectrometer, covering the Raman frequency shift range of ~ -140 to 4300 cm^{-1} at a spectral resolution of 4 - 5 cm^{-1}. The samples were observed and Raman spectra recorded with an Olympus 50X, 0.80 NA air objective which produces a laser beam diameter of ~ 3 μm at focus. The power of the laser beam at the sample was set to ~13 mW. Spectral data collection times ranged from <1 minute up to 15 minutes depending upon sample size, Raman scattering efficiency, and intensity (if any) of background fluorescence.

2.6 Circular dichroism (CD) spectroscopy

CD spectra were recorded at room temperature with a 0.2 mm path length cell using a JASCO J-810 spectropolarimeter. Protein samples were re-suspended respectively in Milli Q water, 7.5 mM $CaCl_2$, 4 mM NH_4HCO_3 (pH 8.0), or undersaturated 0.2 mM $CaCl_2$ plus 4 mM NH_4HCO_3 (pH 8.0) solution (Fu et al., 2005a) to a final concentration of 5 μM, and scanned from 185 nm to 300 nm at 0.1 nm intervals with a scan rate of 20 nm/min. The experimental spectrum represented the average of 5 acquired scans, reported as mean residue molar ellipticity, after the baseline was corrected and the buffer control subtracted. The secondary structure was estimated with CDpro software programs CONTINLL and

CDSSTR, based on the CD spectra from 185 nm to 240 nm, using set 3 as the reference set (Sreerama and Woody, 2000).

2.7 Dynamic light scattering (DLS)

rOC90 was re-suspended respectively in Milli-Q water, 7.5 mM $CaCl_2$, 4 mM NH_4HCO_3 (pH 8.0), or 0.2 mM $CaCl_2$ plus 4 mM NH_4HCO_3 (pH 8.0) that had been filtered using a 0.22 μm membranes, and adjusted to final concentrations of 5 μM and 10 μM. The protein solution was centrifuged at 14,000 rpm for 30 min and transferred to a 12 μl dust-free quartz light scattering microcuvette (1.5 mm). DLS was measured by means of a DynaPro Titan (99-E, MS/XTC) at 20 °C, operating at a wavelength of 825.3 nm. The scattering intensity was recorded at 90 degrees in batch mode and analyzed with a multiple channel digital autocorrelator. The normalized intensity correlation functions were analyzed by the regularization method using the data analysis software package Dynamics V6.2.04. The acquisition time for each run was 10 seconds and the experiment continued for more than 60 runs. Analysis of the correlation function of the whole experiment represents the statistically averaged and thermodynamically stable size distribution of the samples. The theoretical hydrodynamic radii (Rhs) of rOC90 corresponding to 51 kDa (amino acid sequence) and 100 kDa (estimated whole molecule) were calculated according to an hydrodynamic radius (Rh) of $0.475 \times N^{0.29}$ nm for native protein, and an Rh of $0.221 \times N^{0.57}$ nm for denatured protein (Wilkins et al., 1999).

2.8 Molecular modeling

Homology-based models of the two sPLA2-like domains 1 and 2 of OC90 were generated using Swiss Model Server in alignment mode (Schwede et al., 2003). The models of domains 1 and 2 were based on *Micropechis ikaheka* snake venom group IB PLA2 (MIPLA4, Protein Data Bank accession code: 1p7oA), and human group X sPLA2 (hGXPLA2, Accession code: 1le6A) as templates, respectively (Lok et al., 2005;Pan et al., 2002). Alignment between the sPLA2-like sequences with their templates was performed using the T-Coffee program (Version 5.13) (Notredame et al., 2000). Templates were selected based on their high sequence identities. The models were evaluated using Procheck (Laskowski et al., 1993;Laskowski et al., 1993) and Prosa II (Wiederstein and Sippl, 2007;Sippl, 1993) to evaluate the accuracy of the structure. PyMol viewer (V 0.99) (PyMol V0.99, DeLano Scientific, San Francisco, CA) was used to visualize the structures, and PyMol APBS to calculate the surface electrostatic potentials (Baker et al., 2001;Dolinsky et al., 2004).

3. Results

3.1 Preparation and characterization of rOC90 (rOC90)

The HEK293 cell lines stably expressing mouse rOC90 secreted a mature 95 ~ 110 kDa protein. Purification yielded 1.2 - 1.5 mg of protein per batch with a purity of 95% (Fig. 1A). Transient expression of rOC90 tagged with 6xHis residues, yielded a 65 kDa band (15 kDa higher than the protein backbone, consistent with N-glycosylated intracellular rOC90), whereas the 95 - 110 kDa diffuse band represented the mature secreted protein (Fig. 1B). Treatment with N-glycosidase F resulted in a 10 kDa decrease in molecular weight (Fig. 1C). Treatment with alcian blue resulted in distinct staining, indicating the presence of substantial amounts of acidic GAGs (Fig. 1D). Overall, the biochemical characteristics of rOC90 closely conform with native OC90 (Verpy et al., 1999) confirming its validity. The purity of 95% is consistent with *in vitro* crystal growth and solution state studies.

3.2 Interaction of rOC90 with calcite crystals *in vitro*

To model the mechanism by which OC90 interacts with and modifies calcite crystal growth characteristics we added *different* amounts of rOC90 to the $CaCO_3$ growth solution. A significant number of typical rhombohedral calcite crystals were formed under control conditions without addition of *rOC90* (Figs. 2A and 3A). rOC90 added at concentrations of 0.1 - 5 μM and grown for 48 hours resulted in a marked concentration-dependent increase in nucleation density and a progressive decrease in overall crystal size (Figs. 2B-D). Major morphological changes were observed at higher concentrations, including progressive rounding of the acute edges of the (104) faces of the crystals with no changes of the obtuse edges, which resulted in formation of trifaceted end caps (Figs. 3Ab and Bc,e,f). Together, with lengthening and broadening of the crystal bulk, the resulting morphology was similar to that of native mature calcitic otoconia (Fig. 2E). Specificity of this growth pattern was ascertained with serum albumin which induced no morphologic changes, other than minor pitting at high concentrations (Figs. 3Ac and f). Analogous morphological changes have previously been observed upon addition of small molecules, including single aspartic acid, short chains of aspartic acid and acidic peptides (De Yoreo and Dove, 2004;De Yoreo et al., 2007). Recently, analogous changes were observed in the case of the two highly acidic abalone shell proteins, AP8α and β (Fu et al., 2005). (See Discussion.)

3.3 Raman spectroscopy

Confirmation of the polymorph of $CaCO_3$ by Raman spectroscopy was considered indicated because of the major changes in crystal morphology induced by OC90 (Fu et al., 2005a). Crystals grown in pure solution or in the presence of 5 μM rOC90 (Figs. 4A and B) yielded Raman frequency shifts at 281, 712 and 1085 cm^{-1}, characteristic of calcite. The crystals grown in the presence of rOC90 displayed, in addition, a specific frequency shift at 2937.5 cm^{-1}, which is characteristic of carbohydrate-containing organic material, suggesting incorporation of rOC90 into the crystal (J. Freeman, unpublished).

3.4 Primary and secondary structure of mouse OC90

Sequence analysis identified three potential N-glycosylation sites located at Asn 37, Asn 178 and Asn 288 (NetNGlyc 1.0 server), and predicted a site specific for chondroitin sulfate at Ser 222-Gly 223-Glu 224 (Dr. Lijuan Zhang, pers. comm., Fig. 5). Altogether, 23 potential phosphorylation sites are suggested by the NetPhos 2.0 prediction server at a probability higher than 0.9 (Fig. 5). Immuno-blotting of rOC90 using a rabbit anti-phosphorylation protein (Pan) antibody (Invitrogen, Catalog No. 61-8300) suggests the presence of substantial levels of phosphorylation (data not shown). Secondary structure predictions based on PSIPRED indicates a strong preponderance of alpha helical structure, a minor contribution of beta strands plus a major complement of unordered structure. The alpha helices are predicted to be located predominantly at the two sPLA2-like domains (McGuffin et al., 2000).

3.5 Solution state properties of rOC90

Extensive biochemical characterization had established authenticity of primary structure and posttranslational modifications. However, another major concern in the evaluation of recombinant proteins is the adequacy of folding and the size distribution of the macromolecule in solution. For this purpose we relied on solution state studies including CD and DLS.

Circular dichroism is used to establish the distribution of the secondary structure elements of the molecule; moreover, conformational changes due to exposure of the molecule to different ionic solutions can be assessed. These measurements were performed at a rOC90

concentration of 5 μM. Under control conditions in H_2O (Fig. 6) the spectrum shows a prevalence of alpha helical secondary structure, with minima at 208 and 222 nm, and a maximum at 192 nm, as well as a minor contribution of beta sheet structure. The remainder of the molecule consists of unordered structure (see Table I). Exposure to solutions high in calcium and/or carbonate ions resulted in significant changes of secondary structure. Substitution with 7.5 mM Ca^{2+} resulted in a minor decrease of alpha helical and an increase of beta sheet structure, whereas 4 mM NH_4 HCO_3 leads to an increase of both alpha and beta structure. Application of the two substances in combination resulted in an 11.6 % increase of alpha helical structure. Considering the range of wavelengths used, we expect no significant contribution by the glycan moiety to the spectrum (Hornemann et al., 2004). Accordingly, the difference of CD spectra may be attributed to the binding of ions and/or ion clusters to the polypeptide backbone.

DLS provides information about the size distribution of the macromolecule in solution and about its polydispersity. The hydrodynamic radius (Rh) provides an estimate of the size of the molecule including the water. The Rh of rOC90 in water amounts to 3.7 nm at both 5 μM and 10 μM concentrations, which is about 0.9 nm higher than the theoretical Rh of 2.8 nm (corresponding to 474 amino acids). The higher than predicted value is presumably due to the glycan moiety. The mass distribution of rOC90 with an Rh of 3.7 nm amounts to more than 99.7% indicating that rOC90 exists in solution predominantly as homogeneous monomers. Substitution with ionic solutions induced an increase of the Rh from 3.7 nm in H_2O to 6.0 nm in 7.5 mM $CaCl_2$ and 5.1 nm in 4 mM NH_4HCO_3, respectively, and to 5.3 nm in a solution containing 0.2 mM $CaCl_2$ plus 4 mM NH_4HCO_3 (Fig. 7 and Table II).

Comparing the CD and DLS data, we found that the changes in secondary structure of 5 μM rOC90 upon ion binding tended to parallel the changes in Rh (Figs. 6 and 7; Tables I and II), suggesting that conformational changes may contribute to the increased Rh.

3.6 Molecular modeling of OC90

CDS spectra demonstrated that, like its parent molecule sPLA2, OC90 consists predominantly of alpha helical structure and that exposure to solutions high in calcium or carbonate ions induced significant conformational changes. The high similarity of the primary sequence with the appropriate sPLA2 template (MIPLA4) supports the validity of homology-based molecular modeling. Moreover, Pote et al., (1993) have previously applied an analogous approach to structural characterization of otoconin 22, the single domain amphibian homolog of sPLA2.

In order to explore the structural features of the sPLA2-like domains 1 and 2 of OC90 (OC90D1 and 2) to provide insights into the mechanisms underlying modulation of calcite crystal growth, we generated homology-based molecular models of the domains, based on the crystal structures of MIPLA4 and hGXPLA2, respectively (Lok et al., 2005;Pan et al., 2002). Table III summarizes the levels of sequence identity of each model with its template. The Z scores returned by ProCheck (Laskowski et al., 1993) and the G-factors by Prosa II (ProSA-web) (Wiederstein and Sippl, 2007;Sippl, 1993) are indicators of the accuracy of the modeled structures. Considering the presented values (Table III), both models are in a good agreement within the limitations of theoretical structure predictions. (OC90D2 model not shown.)

Figures 8A and D show the surfaces of the modeled sPLA2-like domain 1 (OC90D1). Most conspicuous is the anionic stretch in the lower center of the anterior surface (Fig. 8A). This cluster, consisting of Asp 68, Asp 70, Glu 79, Glu 81, Asp 82 and Glu 85, is encircled by a hydrogen-bonding patch (Thr 72, Asn 73, Gln 74 and Thr 76) and several individual hydrogen-bonding residues (Gln 60, Ser 80, Ser 8 and Ser 66). Figures 8B and C

demonstrate how folding of the indicated loops results in assembly of the anionic cluster which is derived from individual anionic residues and one doublet of the primary sequence. An analogous folding strategy is used for segregation of the hydrogen-bonding donor-acceptor residues from the anionic cluster. A conspicuous number of cationic residues alternating with nonpolar residues form the most peripheral zone.

Another smaller anionic cluster is formed at the right margin of the anterior surface (Glu 51, Glu 52, Glu 55 and Asp57), separated from the central cluster by a proline residue. The surface of the larger putative active region is essentially flat in the picture plane, but the plane of the right hand cluster is inclined by about 90 degrees.

Figure 9 (right column) indicates that most of the anterior surface of OC90D1 is characterized by negative electrostatic polarization, which contrasts the near neutral to positive electrostatic surface of the corresponding template (MIPLA4).

4. Discussion

4.1 rOC90 and structural characteristics

For a proper appreciation of the present study, it should be kept in mind that the experimental data reflect the activity of the whole, highly complex macromolecule, and provide no information about the locations of active sites/regions – information essential to explain the mechanisms underlying the observed phenomena. Likewise, the solution state studies on secondary structure provide only global information about the whole molecule. The logical follow-up strategy would involve increasing resolution by separating and evaluating individual domains, and assessing the role of the different post-translational modifications. This, of course, would represent a long term effort. There are, however, alternate ways of obtaining functionally relevant information. Indirect evidence about mechanisms can be obtained by analysis of primary sequence with respect to potential mineral-interactive regions, computer-assisted predictions of secondary structure, etc. The most important tool, however, is molecular modeling of the sPLA2-like domains. Two factors account for the high validity of the molecular models: 1.The high sequence identity of the sPLA2-like domains with the respective parent molecule, and 2. availability of the crystal structure of both parent molecules to serve as templates (Fig. 9; see sections 2.8 and 3.6, and Table III).

Comparison of the primary structure of OC90 with that of prototypical $CaCO_3$ modulators shows fundamental differences. For instance, the polypeptide backbone of OC90 is considerably less acidic than that of invertebrate $CaCO_3$-modulators in which the aspartic acid content frequently exceeds 50% of the total, and pI values range between 1.5 and 3.0 (Addadi and Weiner, 1985;Politi Y et al., 2007;Takeuchi et al., 2003);(Gotliv et al., 2005). By contrast, OC90 contains only 6% aspartic acid and 8% glutamic acid, and the estimated pI amounts to a modest 4.4. The measured pI of fully modified OC90, however, is much lower (2.9), suggesting that the post-translational modifications (sulfated GAGs, as well as phosphate groups) account for the increased acidity. Another prominent feature of OC90 is the abundance of hydrogen-bonding residues, in particular serine (~10%) (Fig.5). Hydrogen-bonding residues have been shown to act by restructuring of water, desolvation of calcium, and by withdrawing water from biomolecules and lattice, thereby facilitating interaction of calcium and carbonate ions with the mineral phase (Elhadj et al., 2006;Collino and Evans, 2007). This is in contrast to previous models in which anionic, and to a lesser extent cationic residues, were considered the only essential interactants in $CaCO_3$ mineralization.

The two sPLA2 domains of OC90 are considered the principal functional entities of the molecule, an assumption initially based on the analogy with otoconin 22, the major

amphibian matrix protein. Otoconin 22 consists of only a single sPLA2-like domain, yet plays a key role in the mineralization of aragonitic otoconia (Pote et al., 1993). Conservation of the sPLA2-like domains throughout vertebrate phylogeny, from teleost fish to humans, is further support for their functional significance (Petko et al., 2008). Presumably, to adapt the parent sPLA2 for mediation of mineralization, the net number of anionic residues is increased, accompanied by minor clustering in the form of anionic doublets. At the same time, cationic residues are reduced in number, and the enzymatic site is modified and presumed nonfunctional (Pote et al., 1993;Wang et al., 1998;Verpy et al., 1999). However, all disulfide bonds of the parent enzyme are conserved in the sPLA2-like domains, and CD spectra indicate that, as in the two parent sPLA2, alpha helical structure predominates. CD data show significant and consistent conformational changes of OC90 upon exposure to calcium and/or carbonate-rich media, in line with the behavior of related $CaCO_3$ modulators (Fu et al., 2005b).

Conservation of the entire set of disulfide bonds provides the necessary structural stability to OC90D1 and explains why the scaffold of the model is indistinguishable from the crystal structure of the parent molecule (Fig. 9, left column). Moreover, the alpha helices, alongwith beta strands, serve as anchors for the surface loops containing most of the anionic residues, which, upon folding, result in formation of the major anionic clusters on the molecular surface. The loops in question connect beta strands 1 and 2 with the N-terminal part of alpha helix 2 (Figs. 8B and C) and most of the relevant residues are derived from the primary sequence segment displayed at the bottom of Fig. 8. As evident from Fig. 8A, the principal putative active region of OC90D1 extends over a substantial portion of the anterior surface of the molecule and consequently cannot be characterized adequately by linear synthetic peptides. The obvious alternative for characterization of this two-dimensional region consists of site-specific mutagenesis by substituting putative active residues with nonpolar ones. The resulting changes in growth kinetics can subsequently be quantified by molecular scale techniques (De Yoreo et al., 2007).

The significance of tertiary structure in formation of active sites in OC90 is in conflict with the proposition of Evans and collaborators – that unordered structure and absence of tertiary structure is an essential characteristic of $CaCO_3$ modulators (Evans, 2003;Collino and Evans, 2007). Evans' concept, which is valid for most invertebrate $CaCO_3$ -related molecules is supported by numerous quantitative biophysical studies based on biomimetic peptides as proxies. However, in the case of OC90 and the homologous amphibian modulator otoconin 22, tertiary structure is essential (Pote et al., 1993). Two-dimensional putative active regions are also present on the crystal surfaces of other globular vertebrate $CaCO_3$ modulators, including the pancreatic lithostatin and the egg shell proteins, ovocleidin 17 and ansocalcin (Bertrand et al., 1996;Lakshminarayanan et al., 2005). The same applies to homology-based molecular models of the otolith matrix protein (OMP), of teleost fish and the minor otoconial matrix protein fetuin A (Murayama et al., 2002;Lu et al., in prep).

In contrast to the globular domains, biomimetic peptide-based studies should be readily applicable to the characterization of regions with unordered structural elements of OC90 (linker and terminal extensions). Although these regions were originally considered of ancillary nature, the emerging significance of hydrogen-bonding acceptor/donor residues and the role of hydrophilicity, makes reconsideration of a potential functional role necessary (Collino and Evans, 2007). The linker segment, for instance, contains a 25 amino acid hydrophilic stretch with only scattered nonpolar residues. A shorter hydrophilic segment in the C-terminal extension consists predominantly of anionic residues and serine. Moreover, both regions are predicted to be amply phosphorylated (Fig. 5).

4.2 Nucleation

Figure 2 indicates that addition of OC90 to the growth solution leads to a pronounced concentration-dependent increase of nucleation density. These findings should be viewed in the context of the standard “slow diffusion” system utilized. With an initial $CaCl_2$ concentration of 7.5 mM, the level of supersaturation with respect to $CaCO_3$ in the presence of the glass surface is consistent with heterogeneous nucleation of a small number of typical rhombohedral calcite crystals in the absence of biomolecular additives (Fig. 2A). In this case the interfacial energy between a forming crystal nucleus and the solid support is lower than when in contact with the bulk solution. Minor reductions of the interfacial energy have profound effects upon the incubation time for nucleation. Most likely the glass surface affects also the OC90 induced facilitation of nucleation (Figure 2).

The ability of surfaces to lower the interfacial energy should have implications for the formation of otoconia. It is expected, that the biological scaffold provided by otolin-1 exhibits structural and chemical features able to control the location and crystallographic orientation of nucleation, mechanisms presumably enhanced by the soluble modulator OC90. Interaction between OC90 and otolin-1 has been documented experimentally at both the protein level and in the modification of calcite crystals *in vitro* (Lu et al., in prep).

One important unanswered question remains: How is the required supersaturation with respect to $CaCO_3$ established, considering the extremely low calcium activity of bulk endolymph (200 uM) (Salt et al., 1989;Kiss et al., 2006)? In view of the strong negative electrostatic surface polarization of the sPLA2-like domains (Fig. 9) and the negatively charged post-translational modifications, calcium ions should be attracted to the molecular surface, thereby contributing to the generation of localized supersaturation.

Several other mechanisms purported to aid in the elevation of local calcium levels have been proposed (Hughes et al., 2006). These include the globular substance, microvesicles analogous to those of bone (Suzuki et al., 1995), the integral membrane protein otopetrin 1 (Hughes et al., 2007;Hurle et al., 2003), and several proteins associated with the free radical system (Hughes et al., 2006;Kiss et al., 2006;Paffenholz et al., 2004;Nakano et al., 2008).

It is understood that the standard “slow diffusion” system provides only semi-quantitative data, because the level of supersaturation and additives is not constant. For exact quantitative evaluations of growth parameters, etc., “constant composition” techniques are required, preferably combined with molecular scale studies based on atomic force microscopy (Tomson and Nancollas, 1978;De Yoreo and Vekilov, 2003). However, for nonquantitative evaluations and comparisons of crystal growth features, slow diffusion systems are suitable and widely used in biomineral and material science.

As a rule, highly acidic proteins inhibit both nucleation and crystal growth, but absorption on an appropriate surface may facilitate nucleation (Gotliv et al., 2005). Using the standard “slow diffusion” system the recently discovered, highly acidic sea shell protein caspartin was found to inhibit calcite nucleation (Marin et al., 2005). However, the less acidic vertebrate modifiers frequently promote nucleation. Apart from OC90, also the minor matrix protein fetuin A, leads to a marked facilitation of calcite nucleation (Lu et al., in prep.). Fetuin A has long been known to play an important role in inhibition of ectopic apatite formation (Schafer et al., 2003). Also the eggshell protein ansocalcin leads to increased nucleation, but in addition, causes marked crystal aggregation (Lakshminarayanan et al., 2003).

The foregoing discussion refers to the classical crystallization pathway, wherein the crystal polymorph is determined upon nucleation (De Yoreo and Vekilov, 2003). However, the

recent discovery of an alternate crystallization paradigm, based on precipitation of amorphous $CaCO_3$, complicates this issue (Aizenberg et al., 2003;Colfen, 2008b; Politi et al., 2007;Politi et al., 2004). In the alternate crystallization pathway, an initial transient amorphous phase is precipitated and spontaneously transforms into the stable crystal polymorphs aragonite or calcite. Distinctions between the two crystallization paradigms can only be made by molecular scale techniques. However for practical purposes, this is of no consequence, because regardless of the pathway to the crystalline state, a newly formed crystal has distinct characteristics that are well-explained by molecular-scale concepts of crystallization (De Yoreo and Vekilov, 2003;De Yoreo et al., 2007).

4.3 Crystal growth and morphology

Apart from its effects upon nucleation, addition of rOC90 results in a progressive concentration-dependent decrease in crystal size, indicating inhibition of crystal growth. Moreover, higher concentrations of the additive induce pronounced changes in crystal morphology. Most conspicuous are the changes at the (104) crystal faces, with rounding of acute edges in the absence of modifications of obtuse edges, thereby resulting in formation of tri-faceted end caps (Fig. 3Ab). These changes, together with lengthening and broadening of the crystal bulk, result in morphology similar to that of mature calcitic otoconia (Figs. 3Ab and E).

To explain the mechanisms underlying morphologic modification by biomolecular additives, the stereochemical recognition paradigm was proposed (Addadi and Weiner, 1985;Addadi et al., 1989);(Mann, 2001). According to this model, the stereochemical characteristics of the biomolecules in question are assumed to closely match the lattice of previously unexpressed crystal faces, whereby they are stabilized. However, systematic atomic force microscopic investigations, combined with computational modeling, demonstrated that stereochemical interaction takes place preferentially at the step edges, rather than at the crystal faces proper (Orme et al., 2001;De Yoreo and Vekilov, 2003).

Fu et al. (2005a) had determined that addition to the growth solution of the highly acidic abalone nacre proteins AP8 alpha and beta resulted in crystal morphology similar to that of mammalian otoconia, analogous to the changes induced by rOC90. In subsequent atomic force microscopic studies the De Yoreo team elucidated the underlying molecular scale mechanism (Fu et al., 2005b). The rounding of the acute edges of the (104) face of calcite crystals was found to be due to acceleration of growth kinetics at the acute step edges relative to the obtuse edges. Acceleration of kinetics was an unprecedented finding since, as a rule, acidic modulators inhibit growth kinetics. Pertinent systematic studies, based on a variety of acidic molecules, ranging from short polyaspartic acid chains and small acidic peptides to AP8α and β, demonstrated that acceleration of kinetics is present only at nanomolar levels, and that kinetics revert to the typical inhibitory pattern at higher concentrations. Whereas inhibition of kinetics by acidic molecules acts by binding to step edges, where they block solute attachment, recent research suggests that acceleration is the result of catalytic processes (Friddle et al., 2010).

The same experimental series confirmed the role of negative charge density in the modulation of growth kinetics and quantified the effects at the molecular scale. The degree of hydrophilicity also had a major effect. The values obtained in linear peptides may provide rough estimates about the potential activity of the anionic stretches on the surface of the globular domains which exhibit comparable negative charges.

As mentioned, calcite crystals, modified by OC90, assume the shape of native mammalian otoconia. This supports the concepts of Mann et al. (1983), that otoconia consist of a complex mosaic of iso-oriented nanocrystallites, ranging in size between 50 - 100

nanometers. Consequently, the composite mineral phase of otoconia reflects the shape of these nanocrystallites and diffracts like a single crystal. It can further be assumed that otolin-1 provides the scaffold capable of organizing the crystallites into iso-oriented assemblies in a process of nano-mesocrystal transformation. Recent biomineral and material science research indicates that mesocrystal transformation is much more widespread in $CaCO_3$ systems than originally realized (Colfen and Mann, 2003;Niederberger and Colfen, 2006;Colfen, 2008;Politi et al., 2008).

4.4. *In vivo* effects of OC90

Zhao et al. (2007) demonstrated that ablation of the OC90 gene results in the formation of a small number of huge, spindle-like calcitic aggregates, rather than “giant otoconia”. As expected, OC90 is absent, but in addition, the corresponding structural protein otolin-1 is not detectable in the otoconial matrix, although it is expressed in the underlying epithelia (Zhao et al., 2007). This indicates that OC90 is responsible for recruitment of otolin-1, in addition to its action as crystal growth modulator. A corresponding mechanism has previously been demonstrated in the otolith of zebrafish (Murayama et al., 2005). It is important, therefore, to realize that the observed abnormalities following OC90 gene ablation may be due to the failure of expression of both, OC90 as well as otolin-1.

Verpy et al. (1999) proposed that the abundant secretion of OC90 into the endolymphatic spaces may affect the developing cochlea. Indeed, OC90 gene ablation resulted in a distinct reduction of the thickness of the tectorial membrane, but preliminary evaluations have not detected any negative effects upon hearing (Zhao et al., 2007).

5. Conclusions

We generated high quality rOC90 based on mammalian expression in amounts sufficient for *in vitro* crystal growth and solution state experimentation. Biochemical and biophysical validation confirmed that the recombinant protein resembles the native molecule in all essential aspects. We demonstrate that rOC90 is a multifunctional molecule which facilitates calcite nucleation, inhibits crystal growth and induces changes in crystal morphology, which result in a shape characteristic of native otoconia, supporting the concept that otoconia constitute mesocrystals. In addition, OC90 is responsible for recruitment of the corresponding structural protein otolin-1. OC90 is considerably less acidic than the prototypical invertebrate $CaCO_3$ – associated protein, but is nevertheless an effective modulator of calcite crystal growth. Based on homology modeling of the sPLA2-like domains of OC90, we propose that the lower density of acidic residues of the primary sequence is compensated by formation of major anionic surface clusters upon folding into tertiary conformation. The present experiments provide no information about the overall conformation of OC90. However, preliminary predictions based on Robetta modeling (not shown) (Chivian et al., 2005;Kim et al., 2004;Simons et al., 1997) suggest that the molecule is arranged in an ovoid conformation, and that its molecular surface is characterized by negative electrostatic polarization (Lu et al. in prep.).

6. Future directions

The successful completion of crystal growth experimentation based on rOC90 opens the door for elucidation of various facets of biologically-controlled mineralization of otoconia. Of particular interest should be extension of our ongoing research on recombinant otolin-1, and further development of otolin-1 oligomers into weblike matrices, analogous to those formed by the close homolog collagen type X. This would enable *in vitro* formation of higher order crystallites resembling the mesocrystal structures of native otoconia. This in turn would represent a biomimetic system ideal for the study of the mechanisms underlying

age-induced otoconial demineralization and ultimately to develop preventive or therapeutic strategies.

Acknowledgments

We thank Dr. Lijuan Zhang for prediction of the chondroitin sulfate site; Dr. Jianbo Wang for providing the mammalian expression vector pcDNA3.1 (+) neomycin; Dr. Carl Frieden for valuable discussion on CD; Dr. Thomas Brett for technical assistance with CD and DLS, and discussion of DLS data. This study was supported by DC 009320 (RT) and DC02236 (DMO) from the National Institute on Deafness and other Communication Disorders, NIH.

Abbreviations

BPV	benign positional vertigo
CD	circular dichroism
DLS	dynamic light scattering
GAG	glycosaminoglycan
OC90	Otoconin 90
Rh(s)	hydrodynamic radius (radii)
rOC90	recombinant OC90
sPLA2	secretory phospholipase A2

7. Reference List

Addadi L, Weiner S. Interactions between acidic proteins and crystals: stereochemical requirements in biomineralization. Proc Natl Acad Sci U S A 1985;82:4110–4114. [PubMed: 3858868]

Addadi L, Berman A, Oldak JM, Weiner S. Structural and stereochemical relations between acidic macromolecules of organic matrices and crystals. Connect Tissue Res 1989;21:127–134. [PubMed: 2691196]

Aizenberg J, Weiner S, Addadi L. Coexistence of amorphous and crystalline calcium carbonate in skeletal tissues. Connect Tissue Res 44 Suppl 2003;1:20–25.

Albeck S, Aizenberg J, Addadi L, Weiner S. Interactions of various skeletal intracrystalline components with calcite crystals. J Am Chem Soc 1993;115:11691–11697.

Baker BR, Garrell RL. G-factor analysis of protein secondary structure in solutions and thin films. Faraday Discuss 2004;126:209–222. [PubMed: 14992408]

Baker NA, Sept D, Joseph S, Holst MJ, McCammon JA. Electrostatics of nanosystems: application to microtubules and the ribosome. Proc Natl Acad Sci U S A 2001;98:10037–10041. [PubMed: 11517324]

Bertrand JA, Pignol D, Bernard JP, Verdier JM, Dagorn JC, Fontecilla-Camps JC. Crystal structure of human lithostathine, the pancreatic inhibitor of stone formation. EMBO J 1996;15:2678–2684. [PubMed: 8654365]

Brahms S, Brahms J. Determination of protein secondary structure in solution by vacuum ultraviolet circular dichroism. J Mol Biol 1980;138:149–178. [PubMed: 7411608]

Chivian D, Kim DE, Malmstrom L, Schonbrun J, Rohl CA, Baker D. Prediction of CASP6 structures using automated Robetta protocols. Proteins 61 Suppl 2005;7:157–166.

Colfen H, Mann S. Higher-order organization by mesoscale self-assembly and transformation of hybrid nanostructures. Angew Chem Int Ed Engl 2003;42:2350–2365. [PubMed: 12783497]

Colfen H. Single crystals with complex form via amorphous precursors. Angew Chem Int Ed Engl 2008;47:2351–2353. [PubMed: 18306202]

Collino S, Evans JS. Structural features that distinguish kinetically distinct biomineralization polypeptides. Biomacromolecules 2007;8:1686–1694. [PubMed: 17381152]

De Yoreo JJ, Vekilov PG. Principles of crystal nucleation and growth. Reviews in Mineralogy and Geochemistry 2003;54:57–93.

De Yoreo JJ, Dove PM. Materials science. Shaping crystals with biomolecules. Science 2004;306:1301–1302. [PubMed: 15550649]

De Yoreo J, Wierbicki A, Dove PM. New insights into mechanisms of biomolecular control on growth of inorganic crystals. CrystEngComm 2007;9:1144–1152.

Dolinsky TJ, Nielsen JE, McCammon JA, Baker NA. PDB2PQR: an automated pipeline for the setup of Poisson-Boltzmann electrostatics calculations. Nucleic Acids Res 2004;32:W665–W667. [PubMed: 15215472]

Elhadj S, De Yoreo JJ, Hoyer JR, Dove PM. Role of molecular charge and hydrophilicity in regulating the kinetics of crystal growth. Proc Natl Acad Sci U S A 2006;103:19237–19242. [PubMed: 17158220]

Erway LC, Purichia NA, Netzler ER, D'Amore MA, Esses D, Levine M. Genes, manganese, and zinc in formation of otoconia: labeling, recovery, and maternal effects. Scan Electron Microsc 1986:1681–1694. [PubMed: 3810031]

Evans JS. Principles of molecular biology and biomacrcomolecular chemistry. Reviews in Mineralogy and Biochemistry 2003;54:31–56.

Friddle RW, Weaver ML, Qiu SR, Wierzbicki A, Casey WH, De Yoreo JJ. Subnanometer atomic force microscopy of peptide-mineral interactions links clustering and competition to acceleration and catastrophe. Proc Natl Acad Sci U S A 2010;107:11–15. [PubMed: 20018743]

Fu G, Qiu SR, Orme CA, Morse DE, De Yoreo JJ. Acceleration of calcite kinetics by abalone nacre proteins. Adv Mater 2005a;17:2678–2683.

Fu G, Valiyaveettil S, Wopenka B, Morse DE. CaCO3 biomineralization: acidic 8-kDa proteins isolated from aragonitic abalone shell nacre can specifically modify calcite crystal morphology. Biomacromolecules 2005b;6:1289–1298. [PubMed: 15877344]

Gotliv BA, Kessler N, Sumerel JL, Morse DE, Tuross N, Addadi L, Weiner S. Asprich: A novel aspartic acid-rich protein family from the prismatic shell matrix of the bivalve Atrina rigida. Chembiochem 2005;6:304–314. [PubMed: 15678422]

Hornemann S, Schorn C, Wuthrich K. NMR structure of the bovine prion protein isolated from healthy calf brains. EMBO Rep 2004;5:1159–1164. [PubMed: 15568016]

Hughes I, Thalmann I, Thalmann R, Ornitz DM. Mixing model systems: using zebrafish and mouse inner ear mutants and other organ systems to unravel the mystery of otoconial development. Brain Res 2006;1091:58–74. [PubMed: 16529728]

Hughes I, Saito M, Schlesinger PH, Ornitz DM. Otopetrin 1 activation by purinergic nucleotides regulates intracellular calcium. Proc Natl Acad Sci U S A 2007;104:12023–12028. [PubMed: 17606897]

Hurle B, Ignatova E, Massironi SM, Mashimo T, Rios X, Thalmann I, Thalmann R, Ornitz DM. Non-syndromic vestibular disorder with otoconial agenesis in tilted/mergulhador mice caused by mutations in otopetrin 1. Hum Mol Genet 2003;12:777–789. [PubMed: 12651873]

Ignatova EG, Thalmann I, Xu B, Ornitz DM, Thalmann R. Molecular mechanisms underlying ectopic otoconia-like particles in the endolymphatic sac of embryonic mice. Hear Res 2004;194:65–72. [PubMed: 15276677]

Kawamata S, Igarashi Y. Growth and turnover of rat otoconia as revealed by labeling with tetracycline. Anat Rec 1995;242:259–266. [PubMed: 7668411]

Kim DE, Chivian D, Baker D. Protein structure prediction and analysis using the Robetta server. Nucleic Acids Res 2004;32:W526–W531. [PubMed: 15215442]

Kiss PJ, Knisz J, Zhang Y, Baltrusaitis J, Sigmund CD, Thalmann R, Smith RJ, Verpy E, Banfi B. Inactivation of NADPH oxidase organizer 1 results in severe imbalance. Curr Biol 2006;16:208–213. [PubMed: 16431374]

Lakshminarayanan R, Kini RM, Valiyaveettil S. Investigation of the role of ansocalcin in the biomineralization in goose eggshell matrix. Proc Natl Acad Sci U S A 2002;99:5155–5159. [PubMed: 11959964]

Lakshminarayanan R, Valiyaveettil S, Rao VS, Kini RM. Purification, characterization, and in vitro mineralization studies of a novel goose eggshell matrix protein, ansocalcin. J Biol Chem 2003;278:2928–2936. [PubMed: 12431998]

Lakshminarayanan R, Joseph JS, Kini RM, Valiyaveettil S. Structure-function relationship of avian eggshell matrix proteins: a comparative study of two major eggshell matrix proteins, ansocalcin and OC-17. Biomacromolecules 2005;6:741–751. [PubMed: 15762638]

Laskowski RA, Moss DS, Thornton JM. Main-chain bond lengths and bond angles in protein structures. J Mol Biol 1993;231:1049–1067. [PubMed: 8515464]

Lok SM, Gao R, Rouault M, Lambeau G, Gopalakrishnakone P, Swaminathan K. Structure and function comparison of Micropechis ikaheka snake venom phospholipase A2 isoenzymes. FEBS J 2005;272:1211–1220. [PubMed: 15720395]

Mann S, Parker SB, Ross MD, Skarnulis AJ, Williams RJ. The ultrastructure of the calcium carbonate balance organs of the inner ear: an ultra-high resolution electron microscopy study. Proc R Soc Lond B Biol Sci 1983;218:415–424. [PubMed: 6136976]

Mann, S. Biomineralization: Principles and Concepts in Bioinorganic Materials Chemistry. Oxford University Press; 2001.

Marin F, Amons R, Guichard N, Stigter M, Hecker A, Luquet G, Layrolle P, Alcaraz G, Riondet C, Westbroek P. Caspartin and calprismin, two proteins of the shell calcitic prisms of the Mediterranean fan mussel Pinna nobilis. J Biol Chem 2005;280:33895–33908. [PubMed: 15994301]

McGuffin LJ, Bryson K, Jones DT. The PSIPRED protein structure prediction server. Bioinformatics 2000;16:404–405. [PubMed: 10869041]

Murayama E, Takagi Y, Ohira T, Davis JG, Greene MI, Nagasawa H. Fish otolith contains a unique structural protein, otolin-1. Eur J Biochem 2002;269:688–696. [PubMed: 11856329]

Murayama E, Herbomel P, Kawakami A, Takeda H, Nagasawa H. Otolith matrix proteins OMP-1 and Otolin-1 are necessary for normal otolith growth and their correct anchoring onto the sensory maculae. Mech Dev 2005;122:791–803. [PubMed: 15905077]

Nakano Y, Longo-Guess CM, Bergstrom DE, Nauseef WM, Jones SM, Banfi B. Mutation of the Cyba gene encoding p22phox causes vestibular and immune defects in mice. J Clin Invest 2008;118:1176–1185. [PubMed: 18292807]

Niederberger M, Colfen H. Oriented attachment and mesocrystals: non-classical crystallization mechanisms based on nanoparticle assembly. Phys Chem Chem Phys 2006;8:3271–3287. [PubMed: 16835675]

Notredame C, Higgins DG, Heringa J. T-Coffee: A novel method for fast and accurate multiple sequence alignment. J Mol Biol 2000;302:205–217. [PubMed: 10964570]

Orme CA, Noy A, Wierzbicki A, McBride MT, Grantham M, Teng HH, Dove PM, DeYoreo JJ. Formation of chiral morphologies through selective binding of amino acids to calcite surface steps. Nature 2001;411:775–779. [PubMed: 11459051]

Paffenholz R, Bergstrom RA, Pasutto F, Wabnitz P, Munroe RJ, Jagla W, Heinzmann U, Marquardt A, Bareiss A, Laufs J, Russ A, Stumm G, Schimenti JC, Bergstrom DE. Vestibular defects in head-tilt mice result from mutations in Nox3, encoding an NADPH oxidase. Genes Dev 2004;18:486–491. [PubMed: 15014044]

Pan YH, Yu BZ, Singer AG, Ghomashchi F, Lambeau G, Gelb MH, Jain MK, Bahnson BJ. Crystal structure of human group X secreted phospholipase A2. Electrostatically neutral interfacial surface targets zwitterionic membranes. J Biol Chem 2002;277:29086–29093. [PubMed: 12161451]

Petko JA, Millimaki BB, Canfield VA, Riley BB, Levenson R. Otoc1: a novel otoconin-90 ortholog required for otolith mineralization in zebrafish. Dev Neurobiol 2008;68:209–222. [PubMed: 18000829]

Politi Y, Arad T, Klein E, Weiner S, Addadi L. Sea urchin spine calcite forms via a transient amorphous calcium carbonate phase. Science 2004;306:1161–1164. [PubMed: 15539597]

Politi Y, Mahamid J, Goldberg H, Weiner S, Addadi L. Asprich mollusk shell protein: in vitro experiments aimed at elucidating function in CaCO3 crystallization. CrystEngComm 2007;9:1171–1177.

Politi Y, Metzler RA, Abrecht M, Gilbert B, Wilt FH, Sagi I, Addadi L, Weiner S, Gilbert PU. Transformation mechanism of amorphous calcium carbonate into calcite in the sea urchin larval spicule. Proc Natl Acad Sci U S A 2008;105:17362–17366. [PubMed: 18987314]

Pote KG, Ross MD. Each otoconia polymorph has a protein unique to that polymorph. Comp Biochem Physiol B 1991;98:287–295. [PubMed: 1873986]

Pote KG, Hauer CR III, Michel H, Shabanowitz J, Hunt DF, Kretsinger RH. Otoconin-22, the major protein of aragonitic frog otoconia, is a homolog of phospholipase A2. Biochemistry 1993;32:5017–5024. [PubMed: 8494877]

Salt AN, Inamura N, Thalmann R, Vora A. Calcium gradients in inner ear endolymph. Am J Otolaryngol 1989;10:371–375. [PubMed: 2596623]

Schafer C, Heiss A, Schwarz A, Westenfeld R, Ketteler M, Floege J, Muller-Esterl W, Schinke T, Jahnen-Dechent W. The serum protein alpha 2-Heremans-Schmid glycoprotein/fetuin-A is a systemically acting inhibitor of ectopic calcification. J Clin Invest 2003;112:357–366. [PubMed: 12897203]

Schwede T, Kopp J, Guex N, Peitsch MC. SWISS-MODEL: An automated protein homology-modeling server. Nucleic Acids Res 2003;31:3381–3385. [PubMed: 12824332]

Simons KT, Kooperberg C, Huang E, Baker D. Assembly of protein tertiary structures from fragments with similar local sequences using simulated annealing and Bayesian scoring nctions. J Mol Biol 1997;268:209–225. [PubMed: 9149153]

Sippl MJ. Recognition of errors in three-dimensional structures of proteins. Proteins 1993;17:355–362. [PubMed: 8108378]

Sreerama N, Woody RW. Estimation of protein secondary structure from circular dichroism spectra: comparison of CONTIN, SELCON, and CDSSTR methods with an expanded reference set. Anal Biochem 2000;287:252–260. [PubMed: 11112271]

Suzuki H, Ikeda K, Takasaka T. Biological characteristics of the globular substance in the otoconial membrane of the guinea pig. Hear Res 1995;90:212–218. [PubMed: 8974999]

Takeuchi K, Hatanaka A, Kimura M, Seki N, Kimura I, Yamada S, Yamashita S. Aspolin, a novel extremely aspartic acid-rich protein in fish muscle, promotes iron-mediated demethylation of trimethylamine-N-oxide. J Biol Chem 2003;278:47416–47422. [PubMed: 13129916]

Thalmann R, Ignatova E, Kachar B, Ornitz DM, Thalmann I. Development and maintenance of otoconia: biochemical considerations. Ann N Y Acad Sci 2001;942:162–178. [PubMed: 11710459]

Thalmann I, Hughes I, Tong BD, Ornitz DM, Thalmann R. Microscale analysis of proteins in inner ear tissues and fluids with emphasis on endolymphatic sac, otoconia, and organ of Corti. Electrophoresis 2006;27:1598–1608. [PubMed: 16609936]

Tomson MB, Nancollas GH. Mineralization kinetics: A constant composition approach. Science 1978;200:1059–1060. [PubMed: 17740700]

Veis A. Mineralization in organic matrix frameworks. Reviews in Mineralogy and Geochemistry 2003;54:249–289.

Verpy E, Leibovici M, Petit C. Characterization of otoconin-95, the major protein of murine otoconia, provides insights into the formation of these inner ear biominerals. Proc Natl Acad Sci U S A 1999;96:529–534. [PubMed: 9892667]

Wall RS, Gyi TJ. Alcian blue staining of proteoglycans in polyacrylamide gels using the “critical electrolyte concentration” approach. Anal Biochem 1988;175:298–299. [PubMed: 2469353]

Wang Y, Kowalski PE, Thalmann I, Ornitz DM, Mager DL, Thalmann R. Otoconin-90, the mammalian otoconial matrix protein, contains two domains of homology to secretory phospholipase A2. Proc Natl Acad Sci U S A 1998;95:15345–15350. [PubMed: 9860971]

Wiederstein M, Sippl MJ. ProSA-web: interactive web service for the recognition of errors in three-dimensional structures of proteins. Nucleic Acids Res 2007;35:W407–W410. [PubMed: 17517781]

Wilkins DK, Grimshaw SB, Receveur V, Dobson CM, Jones JA, Smith LJ. Hydrodynamic radii of native and denatured proteins measured by pulse field gradient NMR techniques. Biochemistry 1999;38:16424–16431. [PubMed: 10600103]

Zhao X, Yang H, Yamoah EN, Lundberg YW. Gene targeting reveals the role of Oc90 as the essential organizer of the otoconial organic matrix. Dev Biol 2007;304:508–524. [PubMed: 17300776]

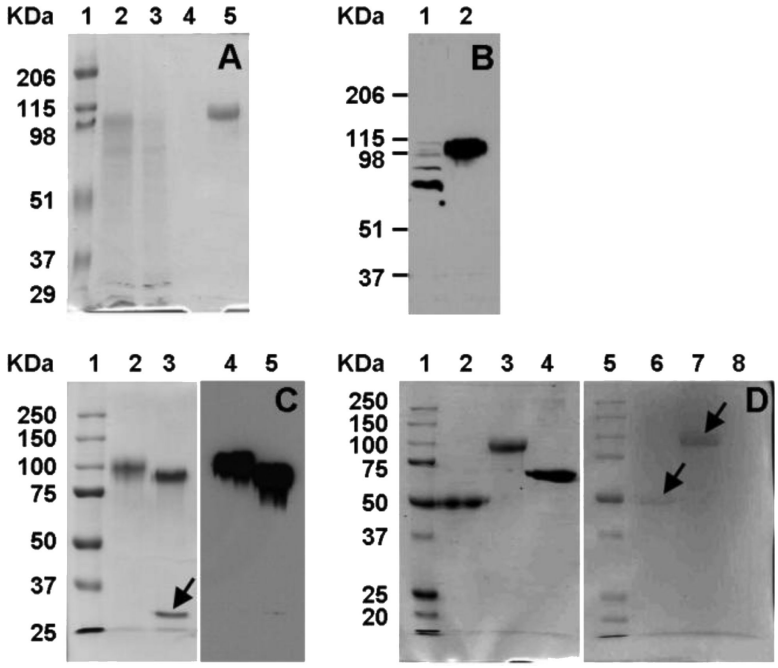

Figure 1. Expression and purification of rOC90 and evaluation of glycosylation

(A) Coomassie blue staining of purification fractions of rOC90. Lane 1. Molecular weight standard; Lane 2: Conditioned serum-free medium; Lane 3: Flow through; Lane 4: Final wash; Lane 5: Elution. (B) Western blot of transiently expressed rOC90 using monoclonal mouse anti-His antibody. Lane 1: intracellular rOC90; Lane 2: secreted rOC90. (C) PNGase F-treated rOC90. Lanes 1-3: Coomassie blue staining; Lanes 4-5: Western blot using polyclonal rabbit anti-mouse OC90 antibody. Lane 1: molecular weight standards; Lanes 2 and 4: rOC90; Lanes 3 and 5: PNGase F-treated rOC90. The PNGase F band is indicated by arrow. (D) GAG analysis of rOC90. Lanes 1-4: Coomassie blue staining; Lanes 5-8: Alcian blue staining. Lanes 1 and 5: Molecular weight standards; Lanes 2 and 6: 3 μg human fetuin A as positive control; Lanes 3 and 7: 3 μg rOC90; Lanes 4 and 8: 3 μg BSA as negative control.

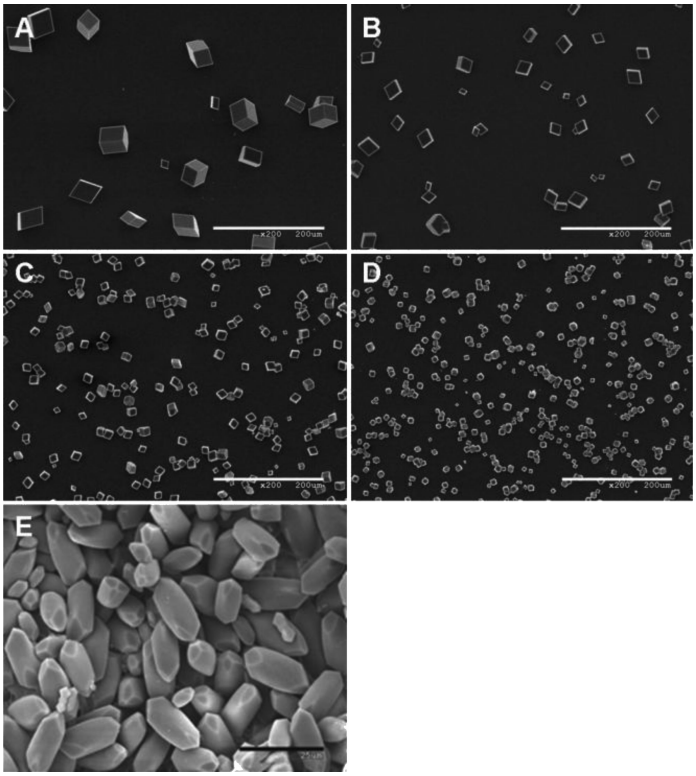

Figure 2. Scanning electron microscopic images of calcite crystals grown in the presence of rOC90

(A) 0 μM. (B) 0.1 μM. (C) 1 μM. (D) 5 μM. (E) Native calcitic otoconia. Scale bars: A - D 200 μm; E 25 μm. Notice dramatic increase of nucleation density and decrease in crystal size due to interaction with rOC90 in a concentration dependent manner.

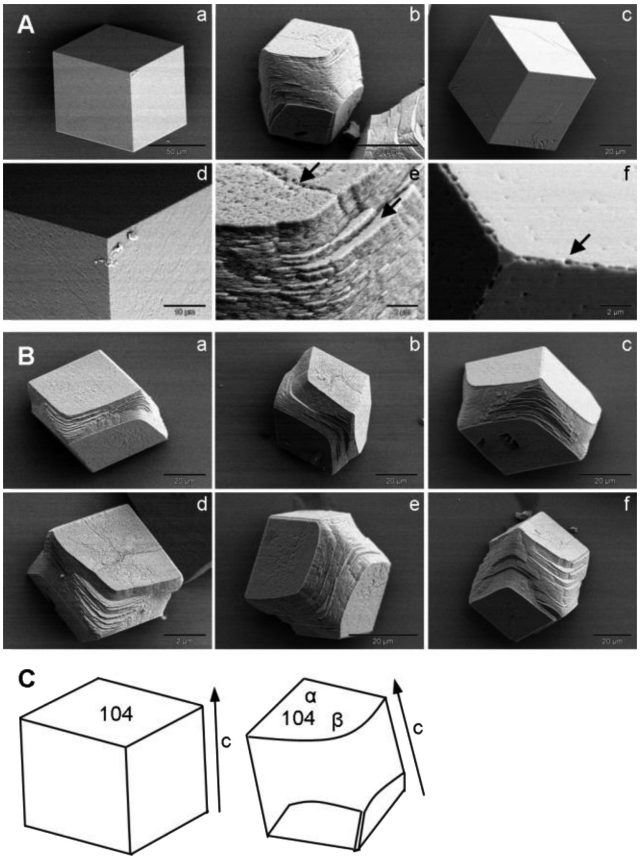

Figure 3. Scanning electron microscopic images of effect of addition of rOC90 upon calcite crystals

(A) a and d: pure solution; b and e: addition of 5 μM rOC90; c and f: addition of 5 μM BSA. Scale bars: a: 50 μm; d: 10 μm; b - c: 20 μm; e-f: 2 μm. Arrows in e indicate perturbation of crystal growth at the acute edges of the (104) face. Arrow in f shows a small pit on the edge of the (104) face. (B) Effect of addition of 5uM rOC90 upon calcite crystals. a - f shows different stages of modification of the acute edges by rOC90 (fully modified crystal shown in panel b of Fig. 3A). Scale bars: a-c, f: 20 μm; d: 2 μm. (C) Computer drawn simulation of crystals a and b of Fig. 3A. The (104) faces are indicated (a and b). α: obtuse angle; β: rounded acute angle. Arrows show direction of c-axis. Pure calcite crystals exhibit typical rhombohedral morphology with six equivalent (104) facets. rOC90 induces rounding of acute edges of adjacent (104) faces, with no changes at the obtuse edges, resulting in trifaceted end caps.

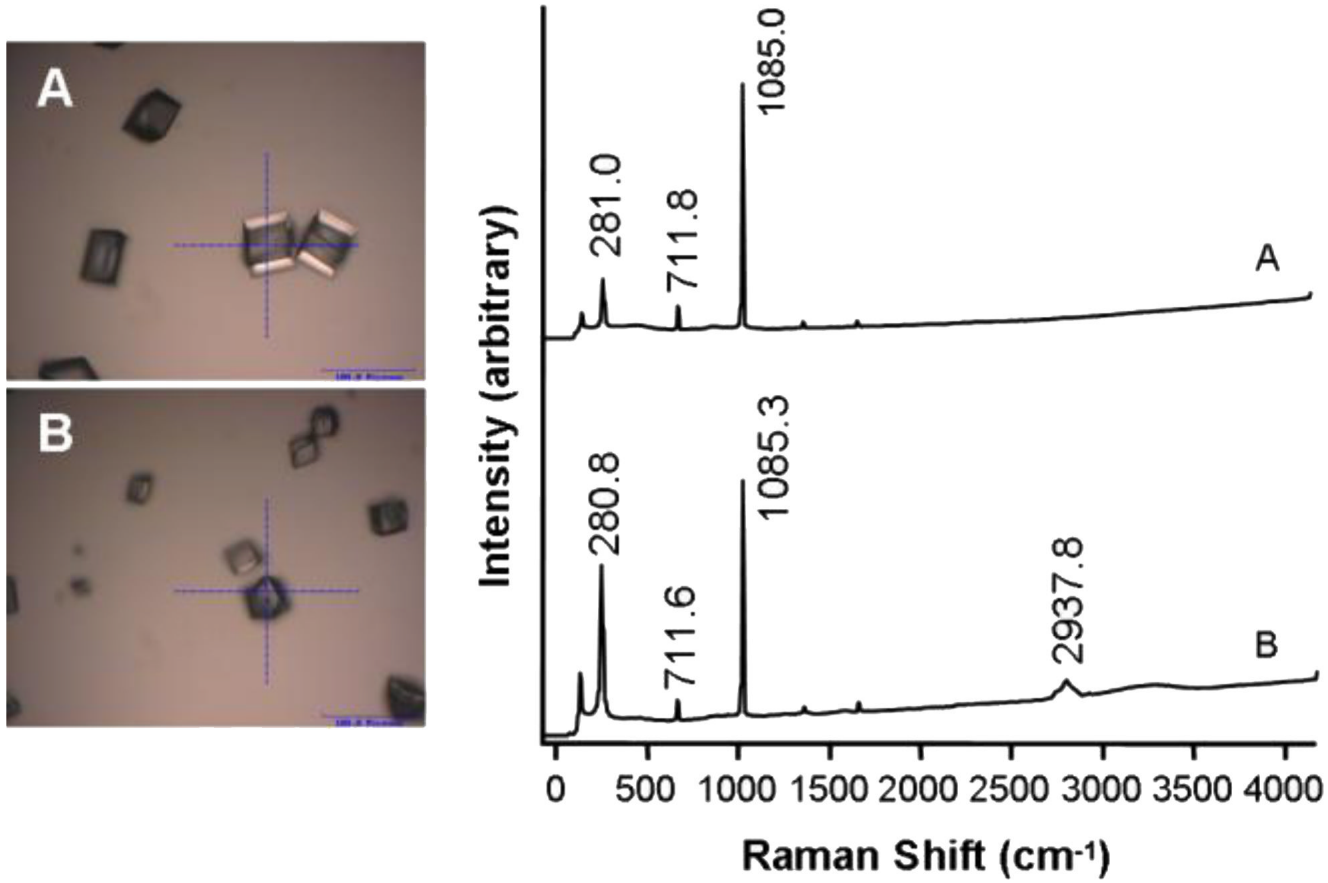

Figure 4. Raman spectra of $CaCO_3$ crystals grown for 48 hours in the presence of 5 μM rOC90

(A) Pure calcite. (B) Addition of 5uM rOC90. Scale bars: A and B, 100 μm. The indicated frequency shifts of 281, 712 and 1085 cm^{-1} are characteristic for calcite. The frequency shift at 2937.5 cm^{-1} was only observed upon addition of rOC90 to the growth solution, suggesting incorporation of the protein into the crystals.

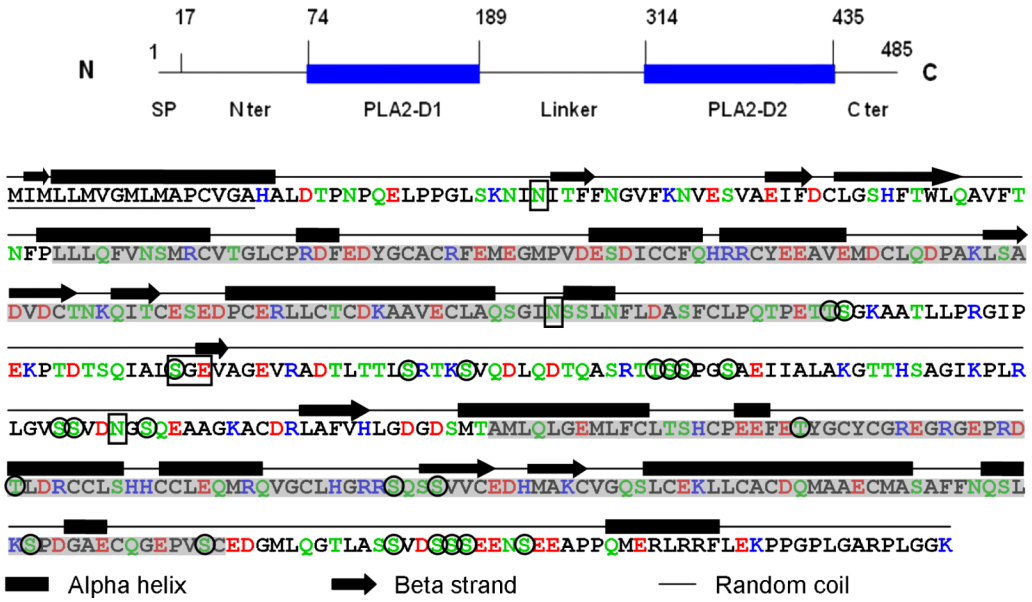

Figure 5. Primary and secondary structure of mouse OC90

The schematic on the top is intended to assist the reader to navigate through the detailed molecule below. The N-terminal 17 amino acid signal peptide is underscored. The two sPLA2-like domains are shadowed. Acidic amino acids: red; basic amino acids: blue; hydrogen-bonding amino acids: green. A 25 amino acids hydrophilic stretch formed by TLTTLSRTKSVQDLQDTQASRTTSS is present in the linker segment. The secondary structure is predicted by the PSIPRED program (McGuffin et al., 2000). The three Asn sites for N-glycosylation predicted by the NetNGlyc 1.0 server, and the chondroitin sulfate site (SGE) predicted by Dr. Lijuan Zhang (pers. comm.) are boxed. The 23 phosphorylation sites suggested by NetPhos 2.0 prediction server are circled.

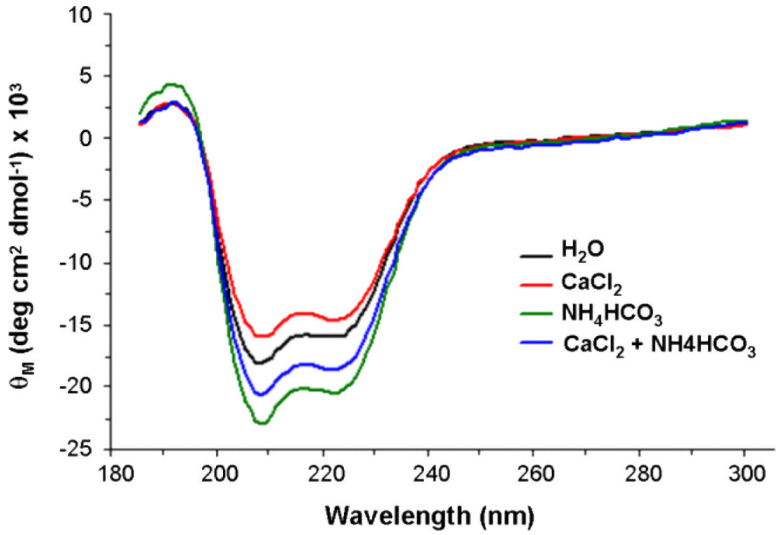

Figure 6. CD spectra of rOC90. The CD spectra were generated by numerical deconvolution analysis

The spectra indicate prevalence of alpha helical secondary structure, with minima at 208 nm and 222 nm, and one maximum at 192 nm. Exposure to Ca^{2+} or HCO3^{-} ions induced characteristic changes of the secondary structure of 5 μM rOC90. 7.5 mM Ca^{2+} (red) causes a slight decrease in alpha helical and increase in beta structure, while 4 mM HCO_3^{-} (green) leads to an increase of both alpha and beta structure. Application of Ca^{2+} and HCO_3^{-1} in combination resulted in an 11.6% increase in alpha helical structure (see Table I).

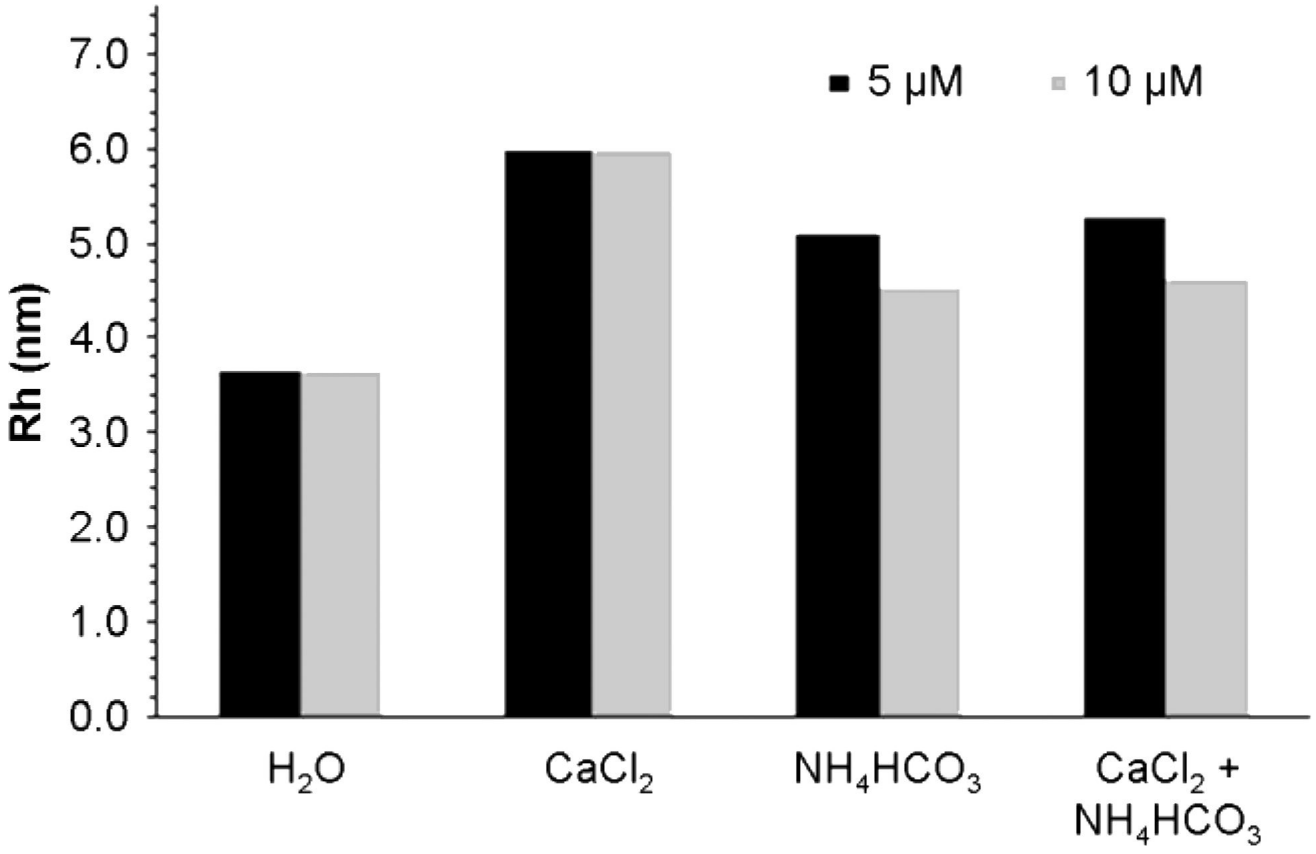

Figure 7. Rhs of rOC90

At both concentrations of rOC90 (5 μM and 10μM, respectively), the Rh in water is 3.7 nm and 6.0 nm in $CaCl_2$. The Rhs of 5 μM and 10 μM rOC90 are 5.1 and 4.3 nm in NH_4HCO_3, and 5.3 and 4.6 nm in a solution undersaturated with respect to $CaCO_3$. The theoretical Rh of rOC90 (474 amino acids) is 2.8 nm for the native protein and 7.4 nm for denatured protein. For corresponding calculated Rhs of rOC90 in various solutions see Table II.

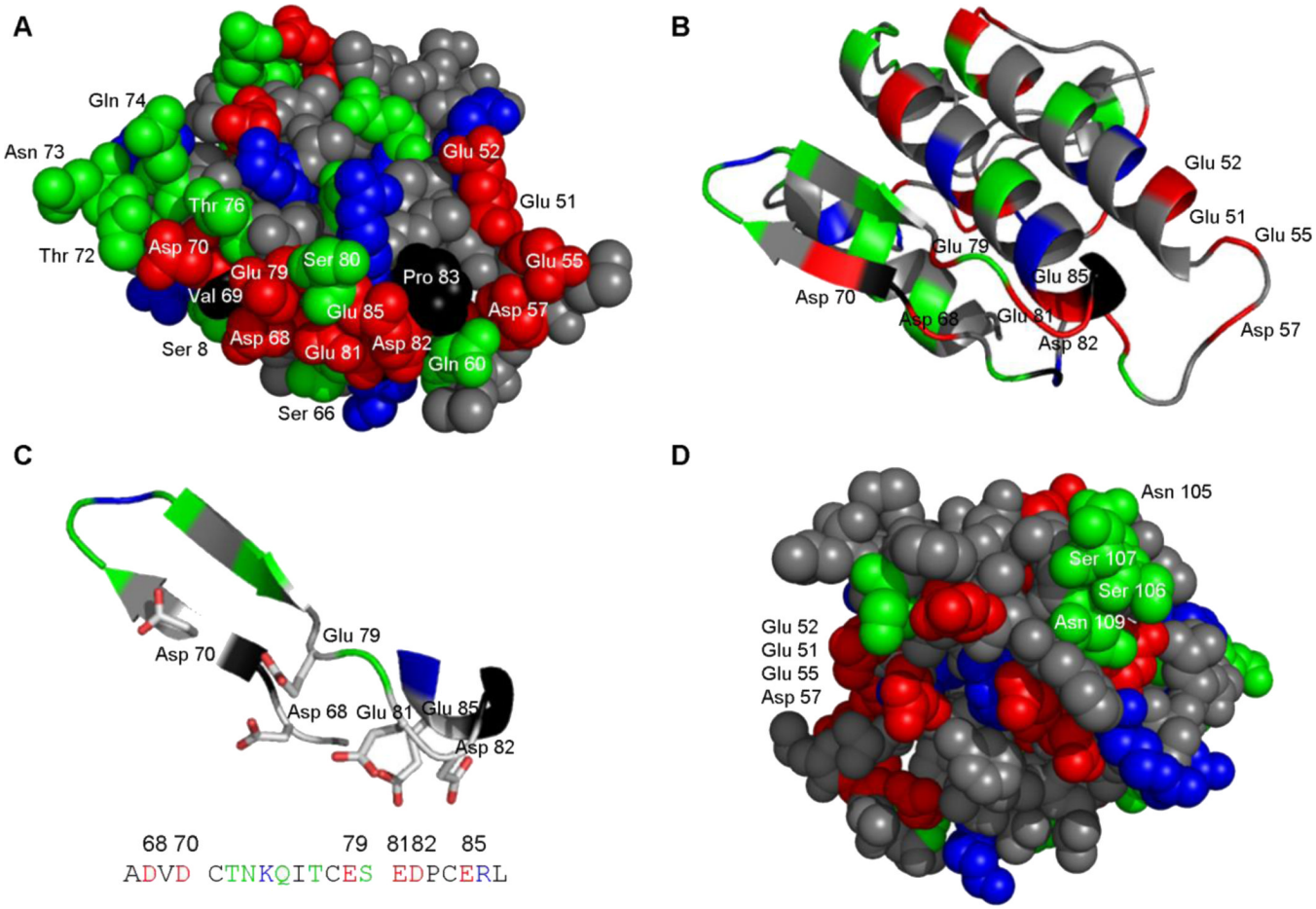

Molecular Model of Mouse OC90 sPLA like domain 1

```
LLLQFVNSMR CVTGLCPRDF EDYGCACRFE MEGMPVDESD ICCFQHRRCY EEAVEMDCLQ 60
DPAKLSADVD CTNKQITCES EDPCERLLCT CDKAAVECLA QSGINSSLNF LDASFC     116
```

Figure 8. Molecular model of sPLA2-like domain 1 of OC90

(A) The homology model of OC90D1 in space filling representation. Two anionic clusters are visible on the anterior surface. The central cluster is formed by Asp 68, Asp 70, Glu 79, Glu 81, Asp 82 and Glu 85 and surrounded by numerous hydrogen-bonding residues. The other anionic cluster, at the right hand margin of the anterior surface is formed by Glu 51, Glu 512, Glu 58 and Asp 57. (B) Cartoon representation in the same orientation as in 8A. (C) Cartoon and sticks representation of the major anionic cluster of 8A. The model shows the tertiary arrangement of the side chains of the acidic amino acids forming the central anionic cluster. (D) A smaller hydrogen-bonding patch is seen on the posterior surface of the model (Asn 105, Ser 106, Ser 107 and Asn 109).

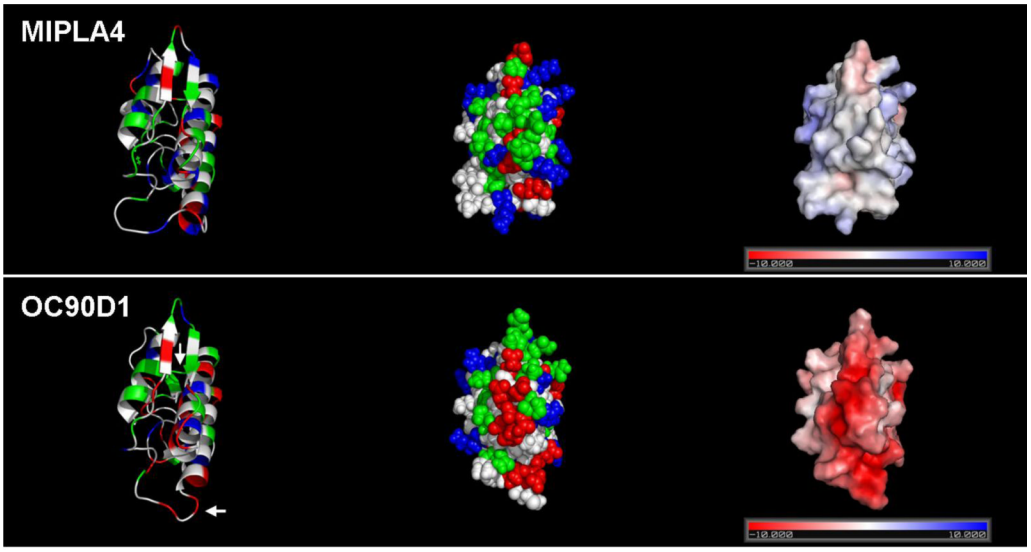

Alignment of OC90D1 with template MIPLA4

```
MIPLA4  NLLQFRNMIKCTIPGREPLLAFSNYGCYCGKGGSGTPVDELDRCCQTHDNCYDKAEKLPE 60
OC90D1  LLLQFVNSMRCV-TGLCPR-DFEDYGCACRFEMEGMPVDESDICCFQHRRCYEEAVEM-D 57

MIPLA4  CKGILSGPYFNTYSYDCTDGKLTCNDQNDKCKLFICNCDRTAAMCFAKAPYNEAYNHFNR 120
OC90D1  C---LQDPAKLSADVDCTNKQITCES-EDPCERLLCTCDKAAVECLAQSGINSSLNFLDA 113

MIPLA4  QLC 123
OC90D1  SFC 116
```

Figure 9. Electrostatics of MIPLA4 and OC90D1

The upper panels represent the crystal structure of the template MIPLA4, the lower panels the homology model of OC90D1. Left column: Cartoon representation; Middle column: space filling representation, Right column: electrostatic surface potential. MIPLA4 and OC90D1 are presented in the same orientation. Loops exhibiting minor differences between the crystal structure of MIPLA4 and the OC90D1 model are identified by arrows. Alignment of respective primary sequences is shown at the bottom of the Figure.

Table I

Secondary structure distribution of rOC90

Solutions	% Distribution of secondary structure features			
	α helix	β sheet	β turn	Unordered
H_2O	49.2	9.2	22.7	18.9
$CaCl_2$	45.5	12.4	20.2	21.9
NH_4HCO_3	59.8	11.5	15.8	12.9
$CaCl_2 + NH_4HCO_3$	55.0	8.9	20.8	15.3

The secondary structure of 5 μM rOC90 in different solutions was predicted using CDpro programs CONTINLL and CDSSTR. The indicated secondary structure estimates represent the combined average of both programs. All normalized root mean square deviations (NRMSD) obtained were less than 11% (data not shown). The NRMSD values reflect the degree of similarity between the experimental and calculated (reconstructed) CD spectra (Brahms and Brahms, 1980). NRMSD values are classified excellent below 5% and acceptable below 15% (Baker and Garrell, 2004). α = alpha helix; βs = beta sheet; βt = beta turn; U = unordered.

Table II

Rhs (nm) of rOC90

rOC90	H_2O			$CaCl_2$			NH_4HCO_3			$CaCl_2$ + NH_4HCO_3		
Rh	Pd%	M%	Rh	Pd%	M%	Rh	Pd%	M%	Rh	Pd%	M%	
5.0 μM	3.7	10.5	99.7	6.0	14.0	99.9	5.1	5.7	99.6	5.3	4.1	99.6
10.0 μM	3.7	11.8	99.7	6.0	16.2	99.4	4.5	19.7	99.8	4.6	16.4	99.7

The Rhs of 5 μM and 10 μM rOC90 were calculated by regularization analysis of the DLS measurements using DYNAMIC V6.2.04 software (Pd %: percentage of polydispersity; M %: percent of mass). rOC90 in H_2O has an Rh of 3.7 nm at both concentrations, slightly higher than the theoretical Rh of 2.8 nm corresponding to 474 amino acids. The mass distribution of Rh values of less than 7.0 nm accounts for more than 99.4%, suggesting that rOC90 is present as homogenous monomer. The minimal aggregation corresponds to Rh values between 16 and 73.7 nm (data not shown).

Table III

Quality assessment of molecular models of OC90

OC90 domain	Identity %	Z score	Overall G-factor
OC90D1	35.77	-6.20	0.00
OC90D2	34.00	-5.27	0.16

Homology of the sPLA2-like domain 1 and 2 with their template are reflected by percent sequence identity. The combined conformational energy of all Cβ-Cβ interactions is reflected by the Z score calculated by PROSA II. Low Z scores indicate favorable conformation. The stereochemical quality of the model is reflected by the Overall G-factor, calculated by Procheck. All G-factors are within the range of theoretical tolerance. High G- factors indicate favorable overall stereochemical geometry.